Readout Current in HZO-Based Bilayer FTJs: Physical Mechanisms and Design Insight

M. Segatto, F. M. Puglisi, *Senior Member, IEEE*, F. Driussi, *Member, IEEE*, D. Lizzit, *Member, IEEE*,
L. Carpentieri, S. Slesazeck, T. Mikolajick, *Fellow, IEEE*, and D. Esseni, *Fellow, IEEE*

***Abstract*— This article establishes a novel interpretation of the readout current in ferroelectric tunnel junctions (FTJs), which we found to be rate-limited by trap-to-trap tunneling (T2T) in the ferroelectric (FE) layer. We show that, with a single set of material parameters, we can reproduce both transient $P - V$ and quasi-static readout experiments for two variants of HZO-based FTJs featuring different tunneling dielectrics. Our investigation puts the simulation of the readout current of FTJs on a much sounder physical basis, which allowed us to then explore a few possible design options to obtain an increase in the readout currents and to improve the ratio between the ON and the OFF currents. Our results suggest that the readout currents can be improved mainly by increasing the bulk trap density in the FE layer.**

***Index Terms*— Ferroelectric devices, ferroelectric materials, memristors, tunneling.**

I. INTRODUCTION

APPLICATIONS of ferroelectric (FE) materials include sensors and actuators, harvesters, and several flavors of electron devices [1]. In particular, the discovery of ferroelectricity in CMOS processing compatible materials, such as fluorite-type $Hf_{0.5}Zr_{0.5}O_2$ (HZO) [2] and wurtzite-type $Al_{1-x}Sc_xN$ [3], has prompted great interest for ferroelectric tunnel junctions (FTJs), ferroelectric FETs (FeFETs) and FE memcapacitors [4], [5], [6]. In this context, FTJs based on a metal–ferroelectric–dielectric–metal (MFDM) stack have been explored as high-impedance memristors in crossbar arrays for in-memory and neuromorphic computing applications [4], [7], [8].

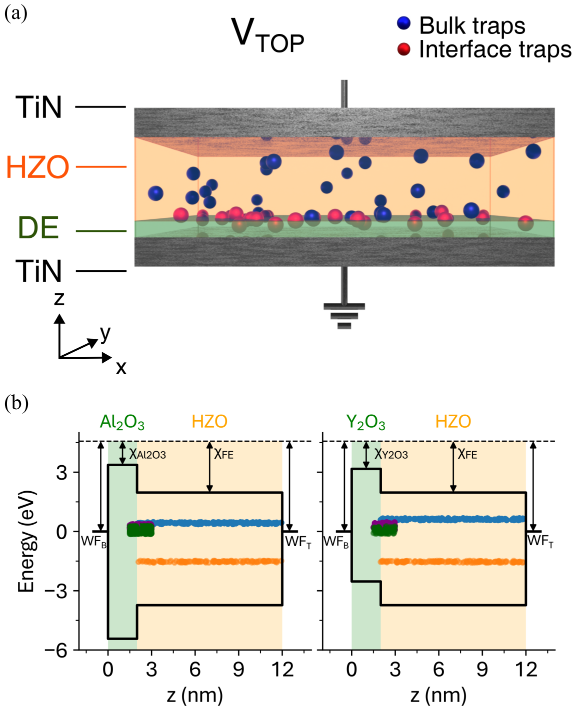

Fig. 1. (a) Sketch of an HZO-based MFDM FTJ, where the DE can be either Al_2O_3 or Y_2O_3. (b) Flat-band diagram for V_{TOP} = 0 V, showing a realization of the energy and spatial distribution of traps according to the parameters in Table I.

A systematic comparison between simulations and experiments has established that charge trapping plays a pivotal role in the stabilization of the FE polarization (P) in MFDM stacks, both in FTJs [9], [10] and in FeFETs [11], [12]. In fact, charge trapping can reduce the FE depolarization field by partly compensating, and thus stabilizing, the FE polarization. The possible role played by traps in the readout current of FTJs, however, has not been investigated in comparable detail. This is also because of the complex physics behind the ON and OFF currents, whereby many co-existing trap-assisted transport mechanisms can contribute to the overall current through the material stack.

In this article, we present a joint simulation and experimental effort where: 1) we identify a single set of material and trap parameters to reproduce both $P - V$ curves, measured with positive-up-negative-down (PUND) experiments, and quasi-

Received 27 November 2025; revised 2 February 2026 and 2 March 2026; accepted 3 March 2026. This work was supported by European Union under Horizon Europe Grant GA:101135398 (FIXIT). The review of this article was arranged by Editor P.-Y. Du. *(M. Segatto and F. M. Puglisi contributed equally to this work.) (Corresponding author: M. Segatto.)*

M. Segatto, F. Driussi, D. Lizzit, and D. Esseni are with DPIA, University of Udine, 33100 Udine, Italy (e-mail: mattia.segatto@uniud.it).

F. M. Puglisi is with DIEF, University of Modena and Reggio Emilia, 41125 Modena, Italy.

L. Carpentieri and S. Slesazeck are with NaMLab gGmbH, 01187 Dresden, Germany.

T. Mikolajick is with NaMLab gGmbH, 01187 Dresden, Germany, and also with the Chair of Nanoelectronics, IHM, 01187 TU Dresden, Germany.

Digital Object Identifier 10.1109/TED.2026.3671219

TABLE I

Trap Parameters Used in the Simulations. The Trap Energy is Referred to the Conduction Band Minimum of the HZO, and Traps are Distributed Uniformly Within the Reported Energy Range, Which is Consistent With Previous Literature [22], [23]. The Volumetric Densities Refer to Bulk Traps Inside the HZO Layer. Interfacial Traps Have Been Described as Traps Actually Distributed in a 1.5-nm-Thick Layer Across the FE–DE Interface, and the Equivalent Areal Densities in the Table are Given by the Corresponding Volumetric Densities Multiplied by the 1.5-nm Thickness. The Densities of Both Bulk and Interface Traps are in Agreement With Values Reported in Literature [24], [25]

FTJ	Al_2O_3-HZO				Y_2O_3-HZO			
Type	Bulk		Interfacial		Bulk		Interfacial	
Cross section σ_T (cm^2)	10^{-14}		10^{-14}		10^{-14}		10^{-14}	
Trap Density	$N_{blk} = 5 \cdot 10^{19}$ (cm^{-3})		$N_{int} = 2 \cdot 10^{14}$ (cm^{-2})		$N_{blk} = 8 \cdot 10^{19}$ (cm^{-3})		$N_{int} = 1.5 \cdot 10^{14}$ (cm^{-2})	
Transition	D(Q) to D(Q-1)	D(Q-1) to D(Q-2)	D(Q) to D(Q-1)	D(Q-1) to D(Q-2)	D(Q) to D(Q-1)	D(Q-1) to D(Q-2)	D(Q) to D(Q-1)	D(Q-1) to D(Q-2)
Energy range (eV)	3.45-3.55	1.5-1.6	1.7-2.1	1.6-2	3.45-3.55	1.3-1.4	1.7-2.1	1.5-1.9
Relaxation Energy (eV)	1.5 ± 0.15	1.5 ± 0.15	1	1	1.5 ± 0.15	1.5 ± 0.15	1	1

static readout $I-V$ characteristics; 2) we demonstrate the role played by traps at the dielectric-ferroelectric (DE-FE) interface during PUND measurements, whereby they can drastically limit the electric field in the DE and the leakage current in the FTJ; and 3) we establish that bulk traps in HZO are crucial for the readout operation, as the current is, in fact, rate-limited by trap-to-trap-tunneling in the HZO layer.

II. Device Fabrication

The MFDM stack was directly deposited onto a p-doped silicon wafer. A titanium nitride (TiN) bottom electrode (BE) was sputtered at room temperature by using a physical vapor deposition (PVD) process, achieving a total thickness of 10 nm. Subsequently, a 10-nm HZO layer and a 2-nm-thin dielectric (DE, Al_2O_3 or Y_2O_3) layer were grown in an OpAL atomic layer deposition (ALD) tool without vacuum break. Finally, a 10-nm-thick TiN top electrode (TE) was sputtered using the same process as employed for the TiN BE [Fig. 1(a)] [13]. To promote the crystallization of HZO, thermal annealing was conducted at 600 °C in a nitrogen atmosphere for 20 s. The capacitor structure, with a radius of 100 μm, was formed through electron beam evaporation of Ti/Pt (10 and 25 nm) using a shadow mask. The fabrication of the entire stack was completed using ion-beam etching to isolate the TE. Grazing incident X-ray diffraction (GIXRD) and X-ray reflectometry (XRR) were used to determine the crystal phases and film thicknesses [13].

III. Simulation Framework

The simulations in this work were performed by using the TCAD simulation tool Ginestra[1], which offers state-of-the-art models for charge transport across DE stacks, and in particular for trap-assisted tunneling (TAT) and trap-to-trap tunneling (T2T) phenomena [14], along with direct tunneling and other transport mechanisms such as the Poole–Frenkel conduction. In our simulations, the dynamic equations for the FE polarization and the charge trapping are solved self-consistently with the Poisson equation, and by duly including in the charge density the contributions due to trapped charges and to the charge states of all defects.

In the device structure sketched in Fig. 1(a), we considered both the design options using either Al_2O_3 or Y_2O_3 as the tunneling DE. As in the fabricated devices, the HZO and DE thickness is, respectively, $t_{FE} = 10$ nm and $t_{DE} = 2$ nm. The relative DE background permittivity of the HZO was set to $\varepsilon_{FE} = 28$, while the permittivity for Al_2O_3 and Y_2O_3 was set to $\varepsilon_{Al_2O_3} = 9$ and $\varepsilon_{Y_2O_3} = 15$, respectively [10], [15]. The electron affinity for the HZO was set to $\chi_{FE} = 2.6$ eV, whereas the electron affinities for the Al_2O_3 and Y_2O_3 were taken as $\chi_{Al_2O_3} = 1.2$ eV and $\chi_{Y_2O_3} = 1.4$ eV, respectively [10], [16]. The tunneling masses for HZO, Al_2O_3 and Y_2O_3 were set to $0.37m_0$, $0.2m_0$ and $0.25m_0$, respectively [10], [17]. While we acknowledge that most oxides are practically amorphous and therefore their effective mass is not well defined, we also argue that, in the context of TCAD models, the tunneling mass is universally used as a semi-empirical material parameter that is calibrated to reproduce the tunneling current across the oxide. The work function (WF) of the TiN contacts is 4.57 eV [18]. The area of each simulated device is 75 × 75 nm^2.

All the main results reported in this article have been obtained by using the symmetric Preisach model to describe the switching of the FE HZO layer. In particular, we used a remnant polarization $P_R = 22.5\,\mu C/cm^2$, a saturation polarization $P_S = 22.55\,\mu C/cm^2$, and a coercive field $E_C = 2$ MV/cm, which are values consistent with previous literature [19]. Moreover, to corroborate the validity of our modeling approach, we will show that similar results can also be obtained by employing the Landau–Ginzburg–Devonshire (LGD) model to describe the FE switching in HZO, and by keeping unaltered the material parameters, the defect densities, and the device geometry. For the simulations based on the LGD model, we used values for the free energy expansion coefficients that are close to those reported in the literature for HZO [10], namely $\alpha = -2.5 \cdot 10^8$ m/F, $\beta = -3 \cdot 10^9 m^5/FC^2$, and $\gamma = 9 \cdot 10^{10}$ m^9/FC^4.

In Ginestra, traps are treated as point-like, discrete sites that can capture one or more electrons and have different charge states. We here employed amphoteric defects that can be found in three charge states. Traps are positively charged when empty [D(Q) initial state], they are neutral when occupied by a single electron [D(Q) to D(Q-1) transition], and are negatively charged when occupied by two electrons [D(Q-1) to D(Q-2) transition].

We included two populations of traps with a different spatial distribution. One population is uniformly distributed in the volume of the HZO, labeled as "Bulk" in Table I, and a

---

[1] Trademarked.

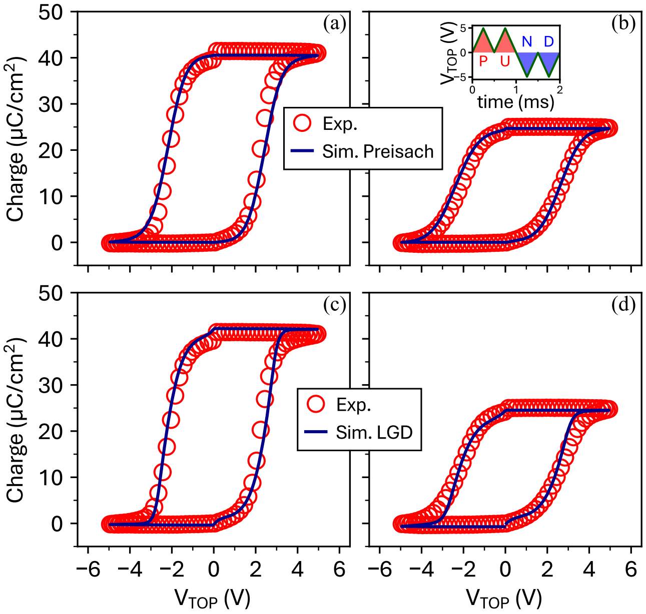

Fig. 2. Charge versus voltage characteristics measured by the PUND method with a 2-ms-long waveform [see inset in (b)] and for (a) Al_2O_3–HZO and (b) Y_2O_3–HZO FTJs (see also Fig. 1). The charge is obtained by subtracting the charges measured during the P (N) and the U (D) pulses, to eliminate possible DC leakage and the paraelectric contribution. Simulations reproduce well the experiments by using the FE and trap parameters given in Section III and Table I. (c) and (d) Same analysis for PUND simulations carried out by using the LGD model for the FE dynamics.

second population is uniformly distributed in a 1.5-nm thick layer across the HZO–DE interface, labeled as "Interfacial" in Table I. Each population plays a significant and different role in the operation of the FTJ devices, as it will be discussed in the next sections. All the trap parameters are summarized in Table I.

For a given set of defects, the discrete traps are randomly generated in the device volume, and the average trap number in the simulation domain is proportional to the trap density, which corresponds to about 10^4 discrete traps in the entire simulated volume. Fig. 1(b) reports the band diagram at $V_{TOP} = 0\,V$ for one realization of the energy and spatial distribution of traps, generated according to the parameters in Table I. Here, we would like to acknowledge that, during a long-term operation of the devices under study, new traps may be generated [20], [21], and the overall properties of traps may statistically change with time. In this work, however, we do not account for the effects of the cycling and aging of the devices. In other words, we assume a fixed trap configuration in the comparison between simulations and experiments that is developed in Section IV.

IV. Comparison With Experimental PUND and Quasi-Static $I - V$

We compared simulations against a complete set of experiments carried out on both the fabricated devices.

A. Analysis of PUND Experiments

We first focus on transient PUND experiments, which we used as a starting point to calibrate the ferroelectricity parameters for the HZO, as well as for the extraction of the parameters of the two trap populations for the Al_2O_3–HZO and the Y_2O_3–HZO FTJs. In fact, as already pointed out in [9], [10], and [26], a high density of traps is required to reproduce the experimental $P - V$ and PUND curves, particularly at the FE-DE interface to reduce the depolarization electric field [26]. Fig. 2 reports the comparison between simulations and measurements for transient PUND performed at a frequency of 500 Hz [see the inset of Fig. 2(b)], showing that our simulations can reproduce experiments quite well once the interface trap distributions are calibrated.

Fig. 2(a) and (b) shows the results for the Al_2O_3–HZO FTJ and the Y_2O_3–HZO FTJ, respectively. As can be seen, the main difference between the two devices is the appreciably different remnant polarization observed in the experiments. Consequently, for the simulations of the Y_2O_3-HZO FTJ, in the Preisach model, we lowered P_R to $12.5\,\mu C/cm^2$ and P_S to $12.55\,\mu C/cm^2$, whereas in the LGD model, we modified the free energy expansion coefficients to $\alpha = -4 \cdot 10^8\ m/F$, $\beta = -1 \cdot 10^9\ m^5/FC^2$, and $\gamma = 8 \cdot 10^{11}\ m^9/FC^4$.

This difference in the HZO properties between the Al_2O_3-HZO and the Y_2O_3-HZO FTJs may be attributed to the slightly different HZO phase compositions of the two fabricated FTJs. Indeed, even if comparable GIXRD peak features were reported for these devices [13], still some slightly different phase compositions and/or rotated FE domains (not contributing to PUND experiments) may be responsible for the different P_R values probed by the electrical characterization.

Fig. 2(c) and (d) reports the same analysis of the transient PUND measurements performed by using the LGD model for the FE dynamics, instead. As can be seen, the quality of the agreement between simulations and experiments is again quite good. These results confirm that, irrespective of the model used for FE dynamics, the traps play a pivotal role in transient PUND characteristics. Moreover, even if it has been reported that Al_2O_3 tends to form interface dipoles [27], [28], the fairly symmetric positive and negative coercive voltages observed in Fig. 2 suggests that, in the device stacks at study, possible interface dipoles are not strong enough to substantially influence the device operation.

B. Analysis of Readout Current and Transport Mechanisms

Once the FE and DE parameters and the trap distributions at the FE–DE interface have been calibrated, we moved to the analysis of read currents. Fig. 3 reports the quasi-static readout currents for both the Al_2O_3–HZO and the Y_2O_3–HZO devices. The I_{OFF} curve (blue) is measured after a RESET pulse, whereas the I_{ON} curve (red) is obtained after a SET pulse. The SET and RESET pulses are identical to the P pulse and the N pulse of the PUND signal, respectively [see inset of Figs. 2(b) and 3(a)].

Because of the inherently statistical distribution of the position and energy of the traps, the simulation of a device having a given set of trap densities corresponds in fact to one specific realization of all the possible devices having such trap densities. Therefore, for each bias point in Fig. 3, the shaded

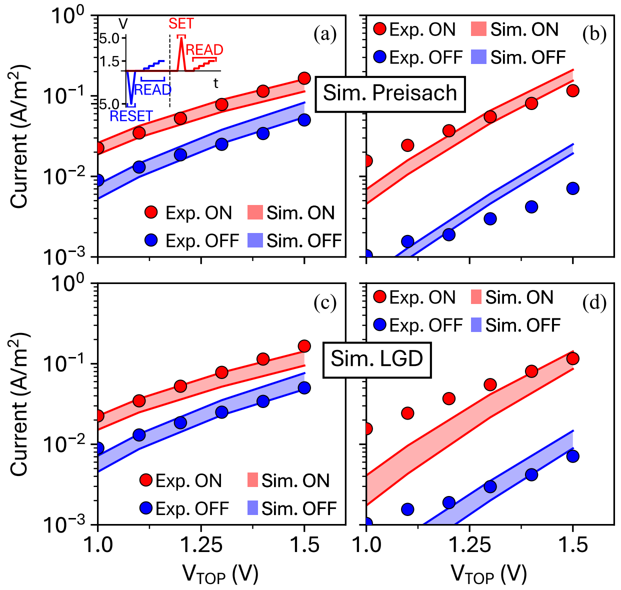

Fig. 3. Comparison between experiments (circles) and simulations (lines) for quasi-static readout currents. OFF current is measured after a RESET pulse and ON current after a SET pulse (see inset). Twenty-five different realizations of the device are simulated, and the shaded area shows the statistical deviation of the results. (a) Experiments and simulations for the Al_2O_3 FTJ. (b) Same comparison for the Y_2O_3 FTJ. (c) and (d) Report the same analysis performed by using the LGD model for FE dynamics.

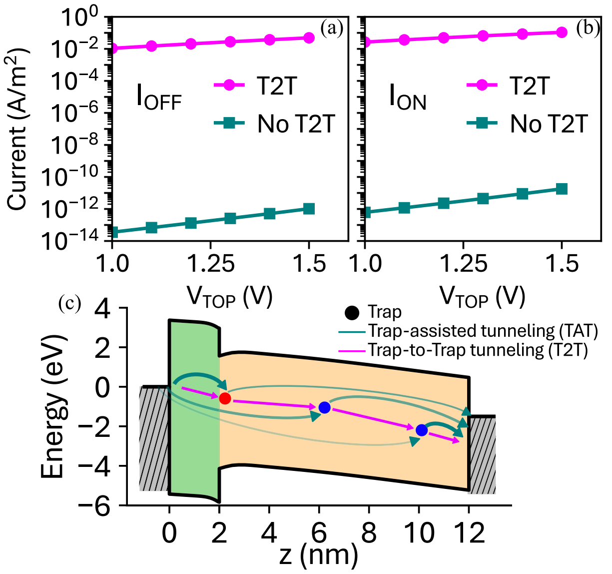

Fig. 4. Simulated readout current calculated by including (T2T) or by excluding (No T2T) the T2T contribution for the Al_2O_3 FTJ. Similar results have been obtained for the Y_2O_3 FTJ (not shown). (a) and (b) Correspond, respectively, to the ON and OFF states already introduced in Fig. 3. (c) Simulated band diagram with a sketch of some trap-assisted-tunneling paths (green arrows) included in our simulations, for electrons moving from the cathode (left, metal contact at the DE layer) to the anode (right, metal contact at the FE layer). The T2T (magenta arrows) can partition the cathode-to-anode tunneling path much more effectively than a mechanism assisted by a single trap TAT [29].

areas correspond to the outcome of 25 independent realizations of a device. More precisely, the shaded area is centered on the current mean value, and the width of the area is equal to two standard deviations of the corresponding results. Proper tuning of bulk trap parameters allowed us to match the experimental $I-V$. Moreover, Fig. 3(c) and (d) reports the same analysis for the readout currents, but performed with the LGD model for the FE HZO.

Quite notably, Figs. 2 and 3 show that, for each device, the same set of material and trap parameters can provide a fairly good agreement with both transient PUND measurements and quasi-static readout currents. This evidence strengthens our confidence in the modeling methodology, particularly because we used essentially the same parameters in the two devices for both interfacial and bulk traps, the only difference being the densities of these defects.

Fig. 4 illustrates the crucial role played by trap-to-trap tunneling in the overall readout current of the FTJs under investigation. In particular, Fig. 4(a) reports the simulated OFF current (for a single device realization), and obtained by either including the trap-to-trap tunneling (T2T, magenta curve) or neglecting it (No T2T, teal curve). When transport does not include T2T, the total current drops by several orders of magnitude, which is consistent with previous results in [21]. Fig. 4(b) shows qualitatively similar results for the ON current.

The prominent role of T2T can be explained with the help of the sketch in Fig. 4(c). In the TAT mechanism, each trap can only exchange carriers with the electrodes, so that each trap can only split into two parts the overall tunneling path between the two electrodes. Therefore, for a TAT mechanism, the dominant contribution to the current is given by the traps located roughly in the center of the DE stack [30], which tends to reduce the TAT current quite drastically when the DE thickness increases. In the T2T mechanism, instead, traps can exchange carriers with other traps, so that the overall tunneling path between electrodes can be split into several shorter subpaths. Therefore, if the density of bulk traps is large enough (i.e., larger than approximately 10^{20} cm^{-3} for the results of this work), the T2T mechanism becomes dominant compared to all other mechanisms included in our simulations, including the Poole–Frenkel transport [14], [31].

Indeed, for a high density of bulk traps in the HZO layer, T2T is the most credible physical mechanism to describe the electronic transport through the FTJ stack [21], [29].

C. Leakage Current During PUND Measurements

Further evidence about the critical role played by traps at the FE–DE interface in the operation of FTJs is shown in Fig. 5(a), where the measured and simulated currents during PUND experiments are compared for the Al_2O_3 FTJs and for different interface trap densities. As can be seen, when a relatively low interfacial trap density $N_{\text{int}} \approx 10^{12}$ cm^{-2} is used in simulations, the calculated current is unrealistically large at high V_{TOP} [green curve in Fig. 5(a)], indeed several orders of magnitude larger than the experimental current (circles). This huge leakage current is drastically suppressed by assuming a higher interface trap density of about 10^{14} cm^{-2} (purple curve), in which case the overall simulated current is in fairly good agreement with experiments.

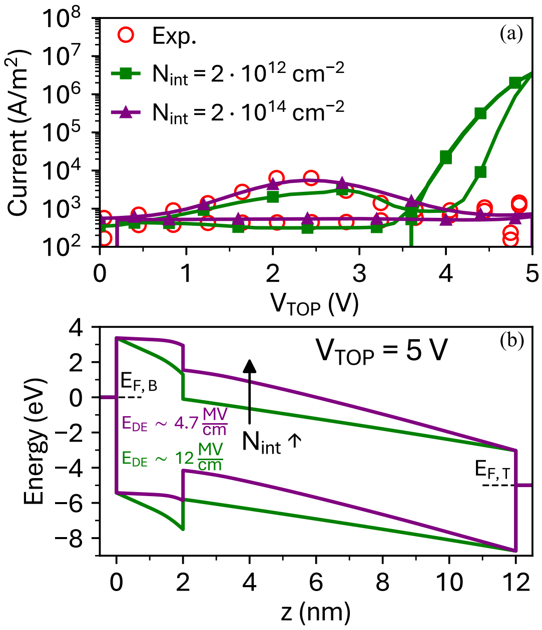

Fig. 5. (a) Simulated and measured current during PUND experiments corresponding to the $P-V$ curve in Fig. 2. For a relatively low density of traps across the HZO–Al_2O_3 interface (10^{12} cm^{-2}), the leakage current at large V_{TOP} (green curve) is orders of magnitude higher than the measured current (open circles). For the trap density in Table I (purple curve), the simulated current is instead in fairly good agreement with experiments. (b) Band diagram in the FTJ for different trap densities at the HZO–Al_2O_3 interface and for V_{TOP} = 5 V. For the lower trap density, the voltage drop across the Al_2O_3 is much larger (green curve) than it is for the higher trap density (purple curve). The large electric field in the Al_2O_3 for N_{int}= 10^{12} cm^{-2} yields the huge leakage current in the simulated curve in (a) (green).

The crucial role played by interfacial traps in the results of Fig. 5(a) is explained in Fig. 5(b), where the energy band diagrams of the stack corresponding to the maximum applied V_{TOP} = 5 V are shown. For the lower trap density (green curve), the band bending in the Al_2O_3 layer is large enough to enable direct tunneling (or even Fowler–Nordheim tunneling) through the thin Al_2O_3 layer. This results in the huge leakage current shown in Fig. 5(a), which is not observed in the experiments. This direct tunneling current triggered by the strong band bending at large V_{TOP} is much larger than the TAT and T2T contributions at the same bias. Furthermore, the electric field in the DE layer corresponding to N_{int}= 10^{12} cm^{-2} appears unrealistic not only because of the huge corresponding currents, but also because such a field would likely induce a breakdown of the thin DE layer [32], [33].

When the interfacial trap density is increased [purple curve in Fig. 5(b)], the electric field in the DE layer is much weaker. For energies close to the Fermi energy $E_{F,B}$ = 0 eV of the bottom electrode (i.e., the cathode), a tunneling current contribution now implies a path inside the HZO bandgap, which drastically reduces the current. The band diagram in Fig. 5(b) also shows a nonlinear band profile in the HZO. This is the outcome of the self-consistent solution of the Poisson and transport equations in the material stack, whereby the charge trapped in the HZO layer results in a nonuniform electric field. Similar results have been obtained for Y_2O_3 FTJs (not shown).

V. ENGINEERING OPTIONS FOR READOUT CURRENT

By leveraging the extensively validated simulation setup described in the previous sections, in this section, we investigate a few design options to increase the readout current and the ratio between the ON and the OFF currents. For this analysis, we used an Al_2O_3-based FTJ as a baseline device, considering the better technological maturity and wider usage in CMOS devices of Al_2O_3 compared to Y_2O_3 based FTJs [34].

In the literature, several attempts have been made to optimize the read current values, for example, by reducing the thickness of the HZO layer to increase the read current [35]. However, recent experimental findings seem to suggest that this design option does not yield the desired results. In fact, by halving the HZO thickness, only a limited increase in the ON-state current could be achieved [20]. Therefore, in this section, we will examine two different design knobs, namely the WF of the metal electrodes and the trap density in the bulk of the HZO layer, which has been shown to depend on the HZO growth process [36], [37].

Fig. 6(a) reports the simulated ON and OFF currents and their ratio for three different WF values. The reduction of WF results in an increase in the current values for both the ON and the OFF states, therefore not improving significantly the I_{ON}/I_{OFF} ratio, as can be seen in Fig. 6(b). This trend qualitatively matches the experimental findings in [38], whereby the WF modulation of the TiN electrodes (obtained by adding a TiAl layer) could improve the current values but at the same time lead to a slightly lower I_{ON}/I_{OFF} ratio.

These results can be explained with the help of Fig. 7, whereby we analyze the band diagrams of the reference device having $WF_T = WF_B = 4.57\,eV$ [Fig. 7(c) and (d)] and of the device having the lowest $WF_T = WF_B = 4\,eV$ [Fig. 7(a) and (b)]. For both the OFF and ON states of the device with WF = 4 eV, the lower WF produces a higher electric field in the HZO layer, as can be seen by comparing Fig. 7(a) and (b) with Fig. 7(c) and (d). Such an influence of WF on the band diagram is basically the same for both the ON and the OFF states; therefore, the I_{ON}/I_{OFF} ratio is hardly affected by the WF, as can be seen in Fig. 6(b).

Besides the influence of the WF of the electrodes, we have also investigated the impact of the density N_{blk} of the HZO bulk traps. Fig. 8 shows that, for t_{FE} = 10 nm, an increase in N_{blk} can enhance the readout current and also push the high I_{ON}/I_{OFF} ratio range to much larger I_{ON} values. This sensitivity to N_{blk} is fully expected, because Fig. 4(a) and (b) has shown that the readout currents are dominated by T2T. Here, it is worth to mention that, for the results in Fig. 8, we have used a fixed density N_{int}= $2 \cdot 10^{14}$ cm^{-2} of interfacial traps which, as pointed out in the caption of Table I, are actually distributed in a 1.5-nm-thick layer across the HZO–DE interface. Therefore, for all the N_{blk} values in Fig. 8, the contribution of N_{blk} to the overall trap density in the 1.5-nm-thick interface region is negligible compared to the contribution of N_{int}. Hence, in the results of Fig. 8, the partial screening and resulting stabilization of the FE polarization is mainly due to interfacial

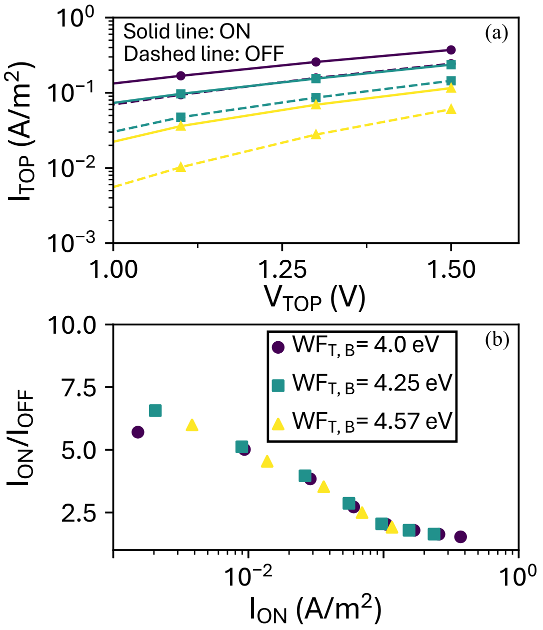

Fig. 6. Simulated quasi-static $I - V$ characteristics for an Al_2O_3-based FTJ having three different WF values $WF_T = WF_B$ (4, 4.25, and 4.57 eV). (a) ON (solid lines) and OFF (dashed lines) current density versus read voltage V_{TOP}. (b) Corresponding ON/OFF ratio versus I_{ON} current.The reduction of WF results in an increase of both the ON and the OFF current; therefore, the I_{ON}/I_{OFF} ratio is essentially unchanged.

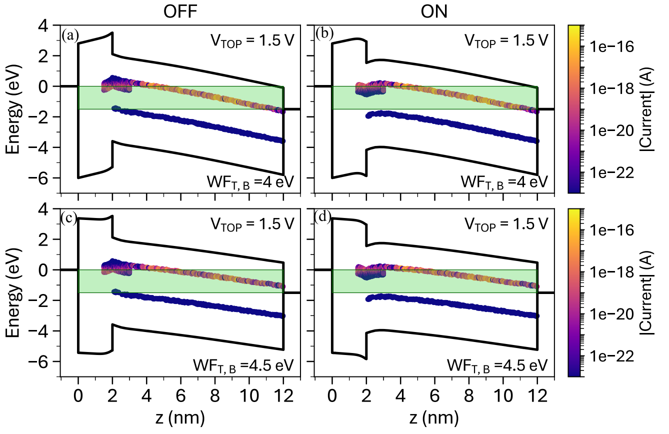

Fig. 7. Band diagrams for the OFF and ON states corresponding to simulations in Fig. 6 and for (a) and (b) $WF_T = WF_B = 4$ eV; and (c) and (d) $WF_T = WF_B = 4.57$ eV. The dots display the discrete trap sites included in the simulations either at the HZO–Al_2O_3 interface or in the bulk of the HZO layer. The contribution of each trap to the total current is illustrated using a color scale. The green shaded area in each plot identifies the Fermi window set by V_{TOP}.

traps, whereas bulk traps are paramount for the electronic transport across the overall DE stack.

One more design knob to tune the performance of the FTJs at study is the thickness of the DE layer [38]. However, the simulated band diagrams reported in Figs. 5(b) and 7 show that, when the FE polarization is sufficiently screened by interfacial traps, then the band bending in the thin DE is quite limited and the readout current is rate-limited by T2T in the HZO layer. In this respect, we verified that moderate changes in the DE thickness cannot change this physical picture for the readout current.

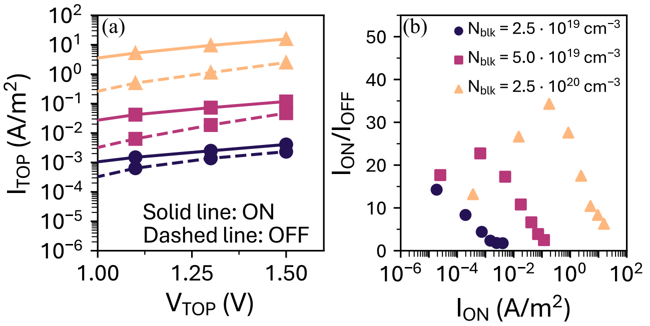

Fig. 8. Simulated readout performance for three different bulk trap densities N_{blk} of an Al_2O_3-based FTJ having t_{FE} = 10 nm. (a) ON (solid lines) and OFF (dashed lines) current densities versus read voltage V_{TOP}. (b) Corresponding ON/OFF ratio versus I_{ON} current. HZO bulk traps play a crucial role in the readout current of the device. An increased trap density leads to higher I_{ON} values and to a slight increase in the ON/OFF ratio.

VI. CONCLUSION

In this article, we report a TCAD simulation framework capable of reproducing both $P - V$ curves from PUND experiments and quasi-static readout $I - V$ characteristics in bilayer FTJs and for two different device variants. Our results emphasize that the operation of bilayer FTJs is largely influenced by both bulk traps in the HZO layer and interface traps at the FE–DE interface. In particular, we demonstrate that the readout current is most likely rate-limited by T2T in the HZO layer, both in the ON and the OFF states. In fact, for readout voltages that do not disturb the polarization state, our simulations suggest that a direct or Fowler–Nordheim tunneling condition through the thin DE is not met.

Then, our calibrated simulation setup has been used to investigate the engineering of the material stack to improve the ON current and I_{ON}/I_{OFF} ratio. Our findings demonstrate that the readout currents can be improved mainly by increasing the density of the HZO bulk traps. The feasibility of these design guidelines remains to be seen, and it is a clear goal for future research activities.

The outcomes of our analysis, together with findings in the literature [21], suggest that a generation of traps induced by cycling or aging is not expected to modify the predominance of T2T in the HZO layer as the tunneling mechanism governing the readout current. However, a systematic analysis of the correlation between device aging and dominant tunneling mechanisms goes beyond the scope of this work, and it constitutes ground for future endeavors.

ACKNOWLEDGMENT

Views and opinions expressed are, however, those of the authors only and do not necessarily reflect those of the European Union or European Commission. Neither the European Union nor the granting authority can be held responsible for them.

REFERENCES

[1] T. Mikolajick et al., “Next generation ferroelectric materials for semiconductor process integration and their applications,” *J. Appl. Phys.*, vol. 129, no. 10, Mar. 2021, Art. no. 100901.

[2] T. S. Böscke, J. Müller, D. Bräuhaus, U. Schröder, and U. Böttger, "Ferroelectricity in hafnium oxide: CMOS compatible ferroelectric field effect transistors," in *IEDM Tech. Dig.*, Dec. 2011, pp. 24.5.1–24.5.4.

[3] S. Fichtner, N. Wolff, F. Lofink, L. Kienle, and B. Wagner, "AlScN: A III-V semiconductor based ferroelectric," *J. Appl. Phys.*, vol. 125, no. 11, Mar. 2019, Art. no. 114103.

[4] S. Slesazeck and T. Mikolajick, "Nanoscale resistive switching memory devices: A review," *Nanotechnology*, vol. 30, no. 35, Aug. 2019, Art. no. 352003.

[5] Y. Ishisaki et al., "Analog memcapacitor by ferroelectric capacitor and its application to spiking neuromorphic system," *IEEE Trans. Electron Devices*, vol. 71, no. 8, pp. 4626–4630, Aug. 2024.

[6] D. Lizzit, M. Segatto, and D. Esseni, "A novel ferroelectric MemCapacitor enabling multilevel operation," *IEEE Trans. Electron Devices*, vol. 72, no. 3, pp. 1083–1090, Mar. 2025.

[7] N. Jao, Y. Xiao, A. K. Saha, S. K. Gupta, and V. Narayanan, "Design space exploration of ferroelectric tunnel junction toward crossbar memories," *IEEE J. Explor. Solid-State Comput. Devices Circuits*, vol. 7, pp. 115–122, 2021.

[8] R. Athle and M. Borg, "Ferroelectric tunnel junction memristors for in-memory computing accelerators," *Adv. Intell. Syst.*, vol. 6, no. 3, Mar. 2024, Art. no. 2300554.

[9] H. W. Park et al., "Polarizing and depolarizing charge injection through a thin dielectric layer in a ferroelectric–dielectric bilayer," *Nanoscale*, vol. 13, no. 4, pp. 2556–2572, 2021.

[10] R. Fontanini et al., "Interplay between charge trapping and polarization switching in BEOL-compatible bilayer ferroelectric tunnel junctions," *IEEE J. Electron Devices Soc.*, vol. 10, pp. 593–599, 2022.

[11] K. Toprasertpong, M. Takenaka, and S. Takagi, "Direct observation of interface charge behaviors in FeFET by quasi-static split C-V and Hall techniques: Revealing FeFET operation," in *IEDM Tech. Dig.*, Dec. 2019, pp. 23.7.1–23.7.4.

[12] S. Deng et al., "Examination of the interplay between polarization switching and charge trapping in ferroelectric FET," in *IEDM Tech. Dig.*, Dec. 2020, pp. 4.4.1–4.4.4.

[13] L. Carpentieri, S. Lancaster, T. Mikolajick, and S. Slesazeck, "Understanding the impact of the dielectric layer in modulating the TER of FTJ devices," in *Proc. IEEE Eur. Solid-State Electron. Res. Conf. (ESSERC)*, Sep. 2024, pp. 408–411.

[14] L. Larcher, A. Padovani, F. M. Puglisi, and P. Pavan, "Extracting atomic defect properties from leakage current temperature dependence," *IEEE Trans. Electron Devices*, vol. 65, no. 12, pp. 5475–5480, Dec. 2018.

[15] A. U. Gehring and S. Selberherr, "Gate current modeling for MOSFETs," *J. Comput. Theor. Nanoscience*, vol. 1, pp. 1–8, 2005.

[16] S. Y. Chiam et al., "Band alignment of yttrium oxide on various relaxed and strained semiconductor substrates," *J. Appl. Phys.*, vol. 103, no. 8, Apr. 2008, Art. no. 083702.

[17] C. L. Hinkle, C. C. Fulton, R. J. Nemanich, and G. Lucovsky, "A novel approach for determining the effective tunneling mass of electrons in HfO_2 and other high-K alternative gate dielectrics for advanced CMOS devices," in *Proc. Microelectronic Eng.*, 2004, vol. 72, nos. 1–4, pp. 257–262.

[18] S. A. Vitale, J. Kedzierski, P. Healey, P. W. Wyatt, and C. L. Keast, "Work-function-tuned TiN metal gate FDSOI transistors for subthreshold operation," *IEEE Trans. Electron Devices*, vol. 58, no. 2, pp. 419–426, Feb. 2011.

[19] A. R. Jayakrishnan, J. S. Kim, M. Hellenbrand, L. S. Marques, J. L. Macmanus-Driscoll, and J. P. B. Silva, "Growth of emergent simple pseudo-binary ferroelectrics and their potential in neuromorphic computing devices," *Mater. Horizons*, vol. 11, no. 10, pp. 2355–2371, 2024.

[20] L. Carpentieri, T. Mikolajick, and S. Slesazeck, "Effect of HZO thickness scaling in the bilayer ferroelectric tunnel junction," *ACS Appl. Electron. Mater.*, vol. 7, no. 11, pp. 5008–5017, Jun. 2025.

[21] L. Benatti, S. Vecchi, M. Pesic, and F. M. Puglisi, "The role of defects and interface degradation on ferroelectric HZO capacitors aging," in *Proc. IEEE Int. Rel. Phys. Symp. (IRPS)*, Mar. 2023, pp. 1–6.

[22] R. A. Izmailov, J. W. Strand, L. Larcher, B. J. O'Sullivan, A. L. Shluger, and V. V. Afanas'ev, "Electron trapping in ferroelectric HfO2," *Phys. Rev. Mater.*, vol. 4, no. 7, Jul. 2020, Art. no. 074607.

[23] R. Izmailov, J. Strand, N. Ronchi, A. Shluger, and V. Afanas'ev, "Electron emission from deep traps in HfO_2 under thermal and optical excitation," *Phys. Rev. B, Condens. Matter*, vol. 109, no. 13, Apr. 2024, Art. no. 134109.

[24] J. Li, M. Si, Y. Qu, X. Lyu, and P. D. Ye, "Quantitative characterization of ferroelectric/dielectric interface traps by pulse measurements," *IEEE Trans. Electron Devices*, vol. 68, no. 3, pp. 1214–1220, Mar. 2021.

[25] D. R. Islamov, V. A. Gritsenko, and M. S. Lebedev, "Determination of trap density in hafnium oxide films produced by different atomic layer deposition techniques," *ECS Trans.*, vol. 80, no. 1, pp. 265–270, Aug. 2017.

[26] M. Segatto, R. Fontanini, F. Driussi, D. Lizzit, and D. Esseni, "Limitations to electrical probing of spontaneous polarization in ferroelectric-dielectric heterostructures," *IEEE J. Electron Devices Soc.*, vol. 10, pp. 324–333, 2022.

[27] M. Pesic, S. Knebel, M. Hoffmann, C. Richter, T. Mikolajick, and U. Schroeder, "How to make DRAM non-volatile? anti-ferroelectrics: A new paradigm for universal memories," in *IEDM Tech. Dig.*, Dec. 2016, pp. 11.6.1–11.6.4.

[28] K.-Y. Hsiang et al., "Bilayer-based antiferroelectric $HfZrO_2$ tunneling junction with high tunneling electroresistance and multilevel nonvolatile memory," *IEEE Electron Device Lett.*, vol. 42, no. 10, pp. 1464–1467, Oct. 2021.

[29] C. Schleich et al., "Single- versus multi-step trap assisted tunneling currents—Part I: Theory," *IEEE Trans. Electron Devices*, vol. 69, no. 8, pp. 4479–4485, Aug. 2022.

[30] E. Vianello, F. Driussi, D. Esseni, L. Selmi, F. Widdershoven, and M. J. van Duuren, "Explanation of SILC probability density distributions with nonuniform generation of traps in the tunnel oxide of flash memory arrays," *IEEE Trans. Electron Devices*, vol. 54, no. 8, pp. 1953–1962, Aug. 2007.

[31] H. Schroeder, "Poole-frenkel-effect as dominating current mechanism in thin oxide films—An illusion?" *J. Appl. Phys.*, vol. 117, no. 21, Jun. 2015, Art. no. 215103.

[32] H. C. Lin, P. D. Ye, and G. D. Wilk, "Leakage current and breakdown electric-field studies on ultrathin atomic-layer-deposited Al_2O_3 on GaAs," *Appl. Phys. Lett.*, vol. 87, no. 18, Oct. 2005, Art. no. 182904.

[33] S. Kim, S.-H. Lee, I. H. Jo, J. Seo, Y.-E. Yoo, and J. H. Kim, "Influence of growth temperature on dielectric strength of Al_2O_3 thin films prepared via atomic layer deposition at low temperature," *Sci. Rep.*, vol. 12, no. 1, p. 5124, Mar. 2022.

[34] B. Max, M. Hoffmann, H. Mulaosmanovic, S. Slesazeck, and T. Mikolajick, "Hafnia-based double-layer ferroelectric tunnel junctions as artificial synapses for neuromorphic computing," *ACS Appl. Electron. Mater.*, vol. 2, no. 12, pp. 4023–4033, Dec. 2020.

[35] B. Max, T. Mikolajick, M. Hoffmann, S. Slesazeck, and T. Mikolajick, "Retention characteristics of $Hf_{0.5}Zr_{0.5}O_2$-based ferroelectric tunnel junctions," in *Proc. IEEE 11th Int. Memory Workshop (IMW)*, May 2019, pp. 1–4.

[36] M. Bai et al., "Regulating ferroelectricity in $Hf_{0.5}Zr_{0.5}O_2$ thin films: Exploring the combined impact of oxygen vacancy and electrode stresses," *J. Appl. Phys.*, vol. 134, no. 17, Nov. 2023, Art. no. 174102.

[37] Y. Choi, H. Park, C. Han, J. Min, and C. Shin, "Improved remnant polarization of Zr-doped HfO_2 ferroelectric film by CF_4/O_2 plasma passivation," *Sci. Rep.*, vol. 12, no. 1, p. 16750, Oct. 2022.

[38] S. Lancaster et al., "Reducing the tunneling barrier thickness of bilayer ferroelectric tunnel junctions with metallic electrodes," in *Proc. Device Res. Conf. (DRC)*, Jun. 2023, pp. 1–2.

Open Access funding provided by 'Università degli Studi di Udine' within the CRUI CARE Agreement